

# Hydrodynamics and Mass Transport in Wall Tube and Microjet Electrodes. 1. Finite Element Simulations

James Melville,<sup>†</sup> Nafeesa Simjee,<sup>‡</sup> Patrick R. Unwin,<sup>‡</sup> Barry A. Coles,<sup>†</sup> and Richard G. Compton<sup>\*,†</sup>

Physical & Theoretical Chemistry Laboratory, Oxford University, South Parks Road, Oxford OX1 3QZ, UK, and Department of Chemistry, University of Warwick, Coventry, CV4 7AL, UK

Received: October 19, 2001; In Final Form: December 18, 2001

We report a general numerical strategy for the simulation of the hydrodynamics and mass transfer at a wall tube electrode based on finite element modeling. Previous empirical and approximate analytical treatments predicting the current as a function of flow rate and cell geometry are critically assessed and shown to have limited *general* applicability. Good agreement between experiment and simulation is found, providing a rigorous basis for future work with these electrodes.

## Introduction

Impinging jet electrodes consist of a jet of electrolyte fired from a cylindrical inlet, submerged in stationary fluid of the same medium. A disk electrode is embedded on a flat surface normal to the flow of the electrolyte jet, which strikes the electrode and spreads radially over the surface. Previous studies have suggested the formation of two different flow regimes near the electrode. First, a stagnation region, where the axial flow becomes radial, extends  $\sim 1.2$ – $2.8$  inlet radii across the flat surface, centered directly below the jet.<sup>1,2</sup> Second, outside the stagnation region is the wall-jet region, where the radial velocity begins to decay.<sup>3</sup> There are two limiting forms of the impinging jet electrode geometry. When the electrode is situated entirely within the stagnation region, it is commonly assumed to be uniformly accessible and this is known as a wall tube electrode (WTE).<sup>4</sup> The radius of the electrode must be much smaller than the radius of the nozzle for this to be the case. When the electrode is much larger than the jet of electrolyte, the electrode will extend into the wall-jet region and is accordingly identified as a wall jet electrode (WJE).<sup>5</sup> The WTE and WJE geometries are illustrated in Figure 1.

The microjet electrode<sup>6</sup> (MJE) is a hydrodynamic ultra-microelectrode (UME) that has been applied to measure fast electrode and homogeneous kinetics.<sup>7,8</sup> In the MJE, solution is fired at high velocity through a capillary positioned over the UME. The radius of the capillary is generally 3–5 times that of the UME, and therefore, the geometry represents a miniaturized version of the WTE, rather than a WJE.

The MJE has, hitherto, employed large UMEs (25  $\mu\text{m}$  diameter), with sufficiently high convective rates that the diffusional edge effect is negligible.<sup>6–8</sup> This, however, limits the conditions under which this novel hydrodynamic UME may be used.

The increasingly wide use of MJEs and WTEs for mechanistic, kinetic, and analytical studies leads to a need to characterize the measured currents in terms of the solution flow rate and cell geometry. In this paper, by means of finite element

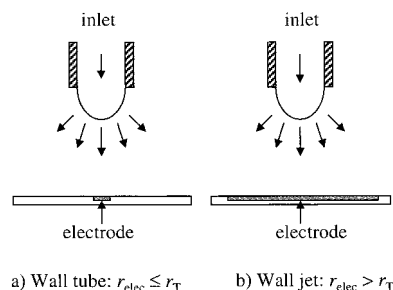


**Figure 1.** The two limiting cases of the impinging jet electrode geometry. In the wall tube electrode (WTE), the radius of the electrode ( $r_{\text{elec}}$ ) is smaller than or equal to the radius of the inlet that produces the impinging jet ( $r_T$ ). In the case of the wall jet electrode (WJE), the radius of the electrode is much larger than that of the impinging jet.

simulation, it will be shown that the existing analytical theory and empirical descriptions of the WTE are of limited applicability, because of intrinsic assumptions that may not be realized in experimental practice. In their place we suggest a generic simulation strategy based on finite element modeling.

## Status and Limitations of Existing Theory

The original treatment of flow impinging on a wall was given by Froessling.<sup>9</sup> The schematic flow pattern inferred to apply, “stagnation in three-dimensional flow”, is shown in Figure 2, where a fluid stream impinges on a wall at right angles to it and flows away radially in all directions.

In the WTE, solution emerges from the inlet of radius  $r_T$  at a volume flow rate,  $V_f$ , and impinges on a disk electrode of radius  $r_{\text{elec}}$ , flowing away radially in all directions.  $r_{\text{elec}}$  must be much smaller than  $r_T$  for the WTE limit to be reached.  $r_{\text{elec}}$  and  $r_T$  are illustrated in Figure 3. The derivation of the Froessling flow profile<sup>9</sup> and subsequent application<sup>4,10</sup> in guiding the wall tube electrode problem involves three simplifying assumptions as follows, the first two of which are related to the hydrodynamics and the third to the mass transport via diffusion and convection:

- (i) A uniform velocity is assumed across the inlet, corresponding to plug flow, before and at the point of entry.
- (ii) As can be seen from Figure 2, a constant radial velocity is imposed at a boundary that extends from the side of the inlet

\* Corresponding author. E-mail: richard.compton@chemistry.oxford.ac.uk.

<sup>†</sup> Oxford University.

<sup>‡</sup> University of Warwick.

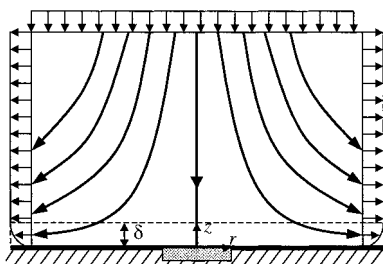


**Figure 2.** A two-dimensional cross section of stagnation in three-dimensional flow—the basis of the analytical solution to the WTE. Outside the hydrodynamic layer the axial velocity,  $u_z$ , and radial velocity,  $u_r$ , are given by the following equations:  $u_r = f'(z)r$  and  $u_z = -2f(z)$ . Inside the hydrodynamic layer, Froessling derived the following equations of velocity:  $u_r = 1.31\alpha^{3/2}\nu^{-1/2}rz$  and  $u_z = -1.31\alpha^{3/2}\nu^{-1/2}z^2$ .

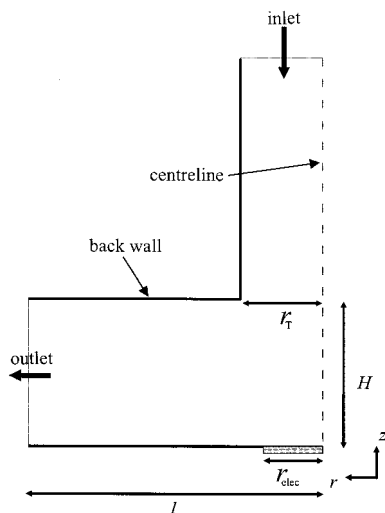


**Figure 3.** Outline of the two-dimensional half-cross-section of the microjet electrode, simulated by FIDAP, with cell parameters marked.

tube down to the edge of the hydrodynamic boundary layer. The latter has a thickness of  $\delta$ .

(iii) Radial diffusion is assumed to be a negligible component of the total diffusive flux to the electrode.

According to Homann,<sup>9</sup> for viscous flow and as in Figure 2, the radial and axial components of the solution velocity,  $u_r$  and  $u_z$ , are given by:

$$u_r = f'(z)r \quad (1)$$

$$u_z = -2f(z) \quad (2)$$

where  $r$  and  $z$  are cylindrical coordinates such that  $r$  is defined as the distance radially from the center of the electrode and  $z$  is the distance in the axial direction.  $f(z)$  is a function defined by the equations of continuity and of motion as reflected in the following third-order partial differential equation:<sup>9</sup>

$$\phi''' + 2\phi\phi'' - (\phi')^2 + 1 = 0 \quad (3)$$

where the primes indicate differentiation with respect to  $\xi$ ,

$$\xi = \sqrt{\frac{\alpha}{\nu}}z \quad (4)$$

and

$$\phi(\xi) = \frac{f(z)}{\sqrt{\alpha\nu}} \quad (5)$$

The parameter  $\alpha$  is a hydrodynamic constant dependent on volume flow rate and  $\nu$  is the kinematic viscosity of the solution. Homann<sup>9</sup> solved eq 3 as a power series in  $\xi$ . Froessling<sup>9</sup> provided an improved numerical solution and showed that close to the electrode, the leading terms are

$$u_r = 1.31\alpha^{3/2}\nu^{-1/2}rz \quad (6)$$

$$u_z = -1.31\alpha^{3/2}\nu^{-1/2}z^2 \quad (7)$$

Homann's work was further developed by Chin and Tsang,<sup>4</sup> who developed an asymptotic solution to the mass transport equation based on the hydrodynamics summarized in eqs 6 and 7 but considered *only normal diffusion*. This showed that the  $r$ -independent mass transport coefficient,  $k$ , is given by

$$k = 0.85002D(\alpha/\nu)^{1/2}Sc^{1/3}g(Sc) \quad (8)$$

where  $D$  is the diffusion coefficient of the species undergoing electron transfer and the Schmidt number is

$$Sc = \nu/D \quad (9)$$

The function  $g(Sc)$  is an asymptotic series in  $Sc$ :

$$g(Sc) = [1 - 0.084593Sc^{-1/3} - 0.0016368Sc^{-2/3} - 0.0057398Sc^{-1} + 0.0014288Sc^{-4/3} + 0.00013088Sc^{-5/3} + \dots] \quad (10)$$

Note that  $g(Sc)$  tends to unity for large  $Sc$ , corresponding to typical electrochemical conditions (for example, in aqueous solution,  $\nu \approx 10^{-2} \text{ cm}^2 \text{ s}^{-1}$  and  $D \approx 10^{-5} \text{ cm}^2 \text{ s}^{-1}$ , giving  $Sc \approx 10^3$ ).

The limiting current at an ideal WTE can readily be calculated as

$$I_{\text{LIM}} = nF\pi r_{\text{elec}}^2 k a_0 \quad (11)$$

where  $n$  is the number of electrons transferred in the redox process, and  $a_0$  is the bulk concentration of the reactant.

In utilizing eq 11 it is important to realize that eq 8 was derived for macroelectrodes, since radial diffusion is neglected in its derivation.

In applying eq 11 to real impinging jets, Chin and Tsang recognized that the flow field outside of the boundary layers depends on the nozzle height,  $H$  (see Figure 3), as well as the nozzle exit flow. To develop eq 11 so as to apply practically, they compiled various literature empirical and "semitheoretical" studies of impinging jet flows, including those with slot rather than circular nozzle geometries, and correlated using a least-squares fitting procedure to show that approximately for laminar conditions

$$k \approx 1.51(D/d)Re^{1/2}Sc^{1/3}g(Sc)(H/d)^{-0.054} \quad (12)$$

where the Reynolds number,  $Re$ , is defined as

$$Re = \hat{U}d/\nu \quad (13)$$

$d$  being the nozzle diameter ( $2r_T$ ) and  $\hat{U}$  the average nozzle exit velocity. Equation 12 was suggested to apply in the ranges  $Re < 2000$  and  $0.1 < r_{\text{elec}}/d < 0.5$ .

It is helpful to reiterate that eq 12 is based on experimental correlation for a macroelectrode geometry, limiting the conditions under which it may apply to the MJE. In particular, any

predictive power in the MJE regime is beyond that anticipated in the original work.

Albery and Bruckenstein<sup>10</sup> have attempted a general treatment of “uniformly accessible electrodes”, reaching similar conclusions to Chin and Tsang with respect to WTEs. They suggested that the term  $H$  in eq 12 contributed “at best a correction of 6% to the value of the limiting current” for the ranges in which it was valid and so, drawing an analogy with the then popular rotating disk electrode, suggested the simplified, further approximated form

$$I_{\text{LIM}} \approx 0.61nF\pi r_{\text{elec}}^2 D^{2/3} \nu^{-1/6} (V_f/r_T^3)^{1/2} a_0 \quad (14)$$

It may be concluded first that eqs 12 and 14 are likely to be reasonable approximations for WTEs, if the geometry covered by the ranges specified above is applicable. Nevertheless, any success these equations might have in predicting the behavior of MJE systems requires significant convective rates, since the latter intrinsically have microelectrode properties.

Also, although eqs 6 and 7 give a good description of the idealized problem shown in Figure 2, it remains the case that no satisfactory description of the flow to a practical WTE has yet been given, as the nozzle exit flow is unlikely to be uniform and, in particular, a uniform radial velocity in the vicinity of the nozzle is unlikely in any real cell, especially if the upper cell wall is at or near the same level as the nozzle. Equally, the location of the cell exits may play a significant role in influencing cell hydrodynamics unless properly designed and positioned.

In the following we present a rigorous treatment of the WTE hydrodynamics and examine the mass transport dependence of the currents flowing at MJEs. First, however, we consider it prudent to verify the original (manual!) calculations of Froessling and Homann, to which we turn in the next section.

### Confirmation of Original Calculations by Froessling

To confirm or otherwise the analytical expressions given in eqs 6 and 7 for the hydrodynamic boundary layer flow corresponding to idealized profile given in Figure 2 as derived by Froessling, eq 3 was solved numerically using the commercial mathematics package Matlab. The following boundary conditions were applied:

$$\zeta = 0: \phi = \phi' = 0$$

$$\zeta \rightarrow \infty: \phi' = 1$$

A graphical solution of eq 3 is given in Figure 4. Tabulated values of  $\phi$ ,  $\phi'$ , and  $\phi''$  obtained by Matlab are compared with those provided by Froessling in Table 1. For all values of  $\zeta$ , the discrepancy between the Froessling and Matlab values of  $\phi$ ,  $\phi'$ , and  $\phi''$  was less than 1%, except in the case of  $\phi''$  at high  $\zeta$ , where  $\phi''$  gets very close to zero. The larger error is presumably a result of rounding errors introduced by Froessling's solution carried out without the aid of a computer.

From Figure 4 and Table 1 it can be seen that, at small values of  $\zeta$ ,  $\phi(\zeta)$  can be approximated by a quadratic of the form

$$\phi = A\zeta^2 \quad (15)$$

A value of  $A$  was calculated by fitting a quadratic to the numerically calculated plot of  $\phi(\zeta)$  at small  $\zeta$ . The values of  $\zeta$  used were at  $\zeta = 3.83 \times 10^{-5}$ ,  $7.66 \times 10^{-5}$ , and  $11.5 \times 10^{-5}$ .

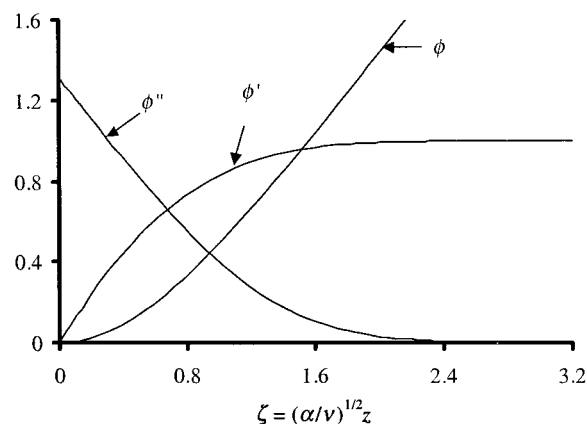


**Figure 4.** Distribution of  $\phi$  plus first and second derivatives with respect to the transformed spatial coordinate  $\zeta$  for the solution of axially symmetrical flow at a stagnation point. The values were calculated using the computer package Matlab.

**TABLE 1: Comparison of Selected Values of Froessling's Manually Generated Solution of Differential Eq 3 (given in the text) and the Values Obtained via Computational Solution**

$\zeta$	Froessling's values			Matlab values		
	$\phi$	$\phi'$	$\phi''$	$\phi$	$\phi'$	$\phi''$
0	0	0	1.3120	0	0	1.3119
0.29	0.0487	0.3311	1.0298	0.0487	0.3310	1.0297
0.57	0.1799	0.5833	0.7563	0.1798	0.5833	0.7562
0.85	0.3717	0.7614	0.5097	0.3716	0.7614	0.5097
1.13	0.6046	0.8761	0.3100	0.6046	0.8761	0.3098
1.41	0.8627	0.9422	0.1676	0.8626	0.9422	0.1675
1.70	1.1346	0.9760	0.0798	1.1344	0.9760	0.0797
1.98	1.4131	0.9912	0.0331	1.4130	0.9911	0.0331
2.26	1.6944	0.9972	0.0120	1.6943	0.9971	0.0119
2.55	1.9769	0.9992	0.0037	1.9767	0.9991	0.0037
2.83	2.2596	0.9998	0.0010	2.2593	0.9996	0.0009
3.11	2.5423	0.9999	0.0003	2.5421	0.9998	0.0002

The approximated quadratic took the form  $\phi = 0.656\zeta^2$ . This confirms the velocity expressions given in eqs 6 and 7.

### Computational Approach

Numerical simulations were carried out with a commercial finite element fluid dynamics software package, FIDAP (version 8.52) (Fluent Europe Ltd., Sheffield, UK, <http://www.fluent.com>), which has been used to successfully investigate other electrochemical systems, such as microwave-heated microelectrodes<sup>11</sup> and flowcells.<sup>12</sup> The program was executed on a Silicon Graphics Origin 2000. The convergence values (used in FIDAP's internal solution software) for each degree of freedom at each node for both the flow and flux problem was set to  $10^{-7}$ . Simulation required 2.5–5 min of CPU time to solve the flow part of the program and 0.5 min for the flux calculation.

### Finite Element Simulation

The finite element approach to simulate the MJE involves constructing a two-dimensional section of the flow domain. An outline of the mesh used with the cell parameters marked is given in Figure 3. FIDAP can treat this model as an axisymmetrical problem, and reports results for the full three-dimensional area of the MJE, created by rotating the two-dimensional cross section about the axis marked as the “centerline”. The ability to apply the solution of a two-dimensional cross section to the full model allows greater accuracy to be achieved in a reasonable computational time.

**TABLE 2: Mesh Edge Parameters Used To Generate the Mesh Faces That Make the Finite Element Mesh in Figure 6**

mesh face	start coordinate, $p_1^a$	end coordinate, $p_2^a$	no. of nodes, $N$	spacing ratio, $q$	paved or mapped meshing?	no. of elements in mesh face
1	$(H, 0)$	$(H + 500, 0)$	51	3	mapped	500
	$(H, r_T)$	$(H + 500, r_T)$	51	3		
	$(H, 0)$	$(H, r_T)$	11	3		
	$(H + 500, 0)$	$(H + 500, r_T)$	11	3		
2	$(25, 0)$	$(H, 0)$	80	5	paved	1917
	$(25, r_{\text{elec}} + 22.5)$	$(H, r_T)$	79	3		
	$(25, 0)$	$(25, r_{\text{elec}})$	51	0		
	$(25, r_{\text{elec}})$	$(25, r_{\text{elec}} + 22.5)$	10	2		
	$(H, 0)$	$(H, r_T)$	11	3		
3	$(0, 0)$	$(25, 0)$	70	50	mapped	3570
	$(0, r_{\text{elec}})$	$(25, r_{\text{elec}})$	70	50		
	$(0, 0)$	$(0, r_{\text{elec}})$	51	0		
	$(25, 0)$	$(25, r_{\text{elec}})$	51	0		
4	$(0, r_{\text{elec}})$	$(25, r_{\text{elec}})$	70	50	mapped	700
	$(0, r_{\text{elec}} + 22.5)$	$(25, r_{\text{elec}} + 22.5)$	70	0		
	$(0, r_{\text{elec}})$	$(0, r_{\text{elec}} + 22.5)$	10	2		
	$(25, r_{\text{elec}})$	$(25, r_{\text{elec}} + 22.5)$	10	2		
5	$(0, r_{\text{elec}})$	$(25, r_{\text{elec}})$	70	50	paved	1804
	$(0, l)$	$(H, l)$	6	0		
	$(25, r_{\text{elec}} + 22.5)$	$(H, r_T)$	79	3		
	$(0, r_{\text{elec}} + 22.5)$	$(0, l)$	49	50		
	$(H, r_T)$	$(H, l)$	30	20		

<sup>a</sup> The coordinates are in units of  $\mu\text{m}$ .

An exact analytical description of the flow in the MJE was obtained by the simulative solution of the Navier–Stokes equations, which are in the form of partial differential equations and, as such, assume that the flow (or flux) domain is represented as a continuum. To solve the problem using the finite element approach, the differential equations are approximated by replacing them with a nonlinear series of algebraic equations that represent the degrees of freedom (e.g., in the case of the flow problem,  $u_r$  and  $u_z$ , and for the flux problem, the flux of electroactive species to the electrode) at a number of nodes (which form the corners of quadrilateral elements) that cover the area of simulation.

The MJE finite element model is made up of five mesh faces. Each mesh face is made up of a series of straight lines (called mesh edges) that define a closed region. Each mesh edge contains a number of nodes. The parameters that define each mesh edge and hence mesh face are defined in Table 2. The length of each mesh edge is defined as the length between two spatial coordinates,  $p_1$  and  $p_2$ . The mesh edge is divided up into a series of intervals,  $N$ , that creates  $N + 1$  nodes. The spacing between the nodes is determined by a ratio,  $q$ . If  $q = 1$ , then the nodes are uniformly spaced. If  $q > 1$ , the distance between the nodes gets progressively larger, with the distance between the last two nodes longer than that of the first two nodes by the  $q$  factor. The ability to provide a gradation of nodes by having some closer together than others is useful when it is necessary to provide a larger number of elements at a certain part of the mesh face, for example, adjacent to the electrode surface.

With the position and number of each node on the mesh edge defined, the nodes are then extended throughout the entire mesh face using the automatic mesh generation capabilities of FIDAP. The positions of the nodal points define the quadrilateral elements that make up the finite element mesh. There are two ways to generate the elements: by mapping or paving.

Mapped meshing requires the mesh face to be quadrilateral and for there to be equal numbers of nodes on the opposing sides of the mesh face. This produces a gridlike set of elements. Paved meshing is generated automatically by FIDAP and is suitable for more complex geometries, as it is unnecessary to meet either of the two requirements stipulated for mapped

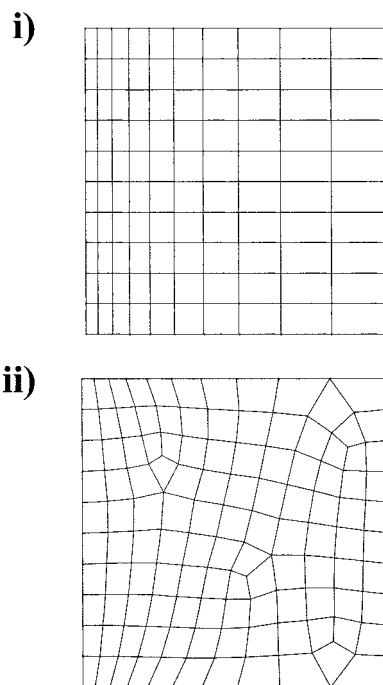


**Figure 5.** An illustration of the two types of meshing available when constructing a finite element model: (i) a mapped mesh and (ii) a paved mesh. Mapped meshing produces a more regular mesh; paved meshing can be applied to less regular areas and can provide a quicker transition from fine to coarse meshing.

meshing. It also provides a transition from fine to coarse elements over a short distance, which is useful to employ under some circumstances. An illustration of the two different forms of meshing over a simple rectangular region is given in Figure 5. There is a slight change from fine- to coarse-sized elements from the left to the right hand side of the mesh face to show the effect of increasing the node density in one part of the mesh face.

Mesh face 1 makes up the nozzle that leads to the MJE cell. It is mapped meshed very coarsely, as the flow profile is expected to take a simple parabolic form in this region. Mesh face 2 is adjacent to mesh face 1 in the  $z$ -direction and almost



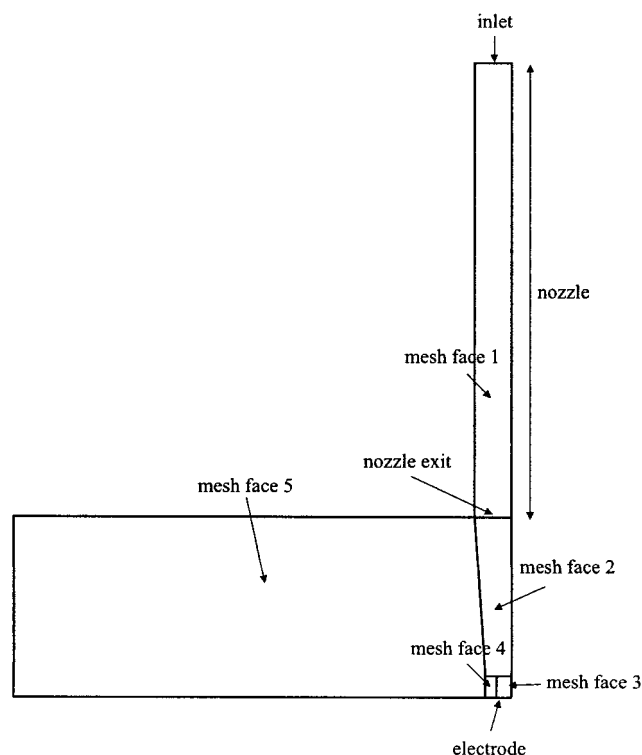


**Figure 6.** Position and shape of the mesh faces used to generate the finite element mesh of the MJE.

extends across the height of the cell. This region represents the area where the solution will have a very high value of  $u_z$  and a small value of  $u_r$ . This region is more densely meshed than the inlet region, as the flow profile is expected to be complicated. This mesh face is paved in order to allow a transition from the coarse meshing at the inlet to the much denser meshing near the electrode. Mesh face 3 is located at and above the electrode surface and extends radially as far as the electrode radius. The mesh here is strongly graded in the  $z$  direction to give a fine mesh adjacent to the electrode surface, where accuracy in the flow profile is most needed. Mesh face 4 is adjacent to mesh face 3 in a radial direction. It was found necessary to provide this region as an intermediate zone between the very finely graded area of the electrode at mesh face 1 to the much more coarsely meshed region toward the outlet, mesh face 5, as without this region, postprocessing of the simulation showed the internal convergence calculations of FIDAP reported larger than average residuals for the solutions of the Navier–Stokes equations at nodes near the electrode, which could lead to errors in describing the flow at the electrode. The solution in the area of mesh face 5 will be, in general, flowing away from the electrode toward the outlet. This region of the MJE cell has little effect on the flow at the electrode and so is coarsely graded. By using paved meshing, far fewer nodes can be used at the mesh edge defining the outlet than those mesh edges closer to

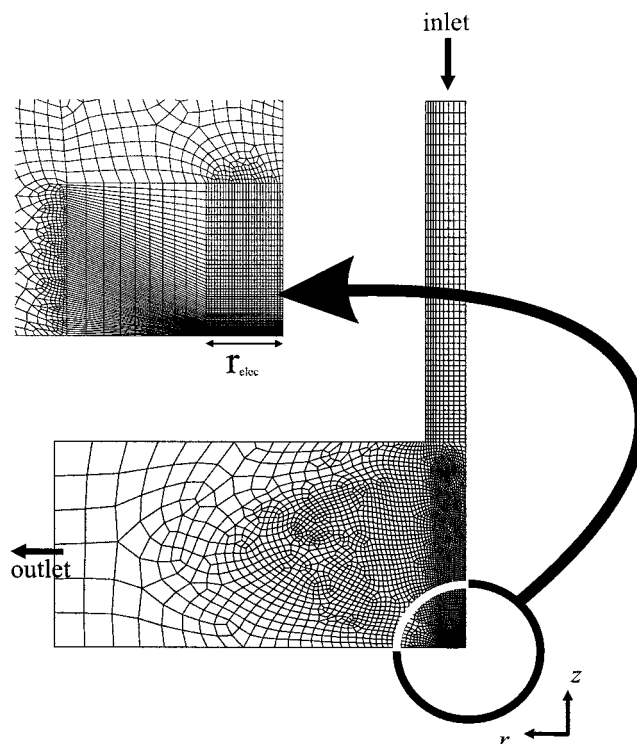


**Figure 7.** Typical finite element mesh used to solve the flow at a MJE. The exact dimensions of each cell simulated in this paper are specified in Tables 3 and 5, but all use the same set of mesh faces and mesh types. The expanded area shows the mesh grading near the electrode.

the electrode, allowing for a smaller number of elements to define this area and thus decreasing the amount of computational time spent on calculating the flow in this relatively unimportant area.

Figure 6 shows the area of the five mesh faces used to generate the two-dimensional cross section of the MJE, and Figure 7 shows the appearance of the fully meshed model, using the values given in Table 2. To obtain “plug” flow, as will be discussed in a subsequent section, mesh face 1 is removed from the model and the inlet is placed where the nozzle exit is marked in Figure 6.

**Flow Simulation.** The finite element simulations were run to model a system as close to physical reality as possible. In particular, in the light of the discussion above, the following realistic possibilities were included to contrast with the idealizations underpinning the derivation of eqs 6 and 7:

- A parabolic velocity distribution was imposed on the flow at the inlet.
- In the finite element solution, for any fixed value of  $r$  between 0 and  $r_T$ ,  $u_r$  is not constrained to a fixed value for all  $z$ .

Boundary conditions as follows were applied to the finite

**TABLE 3: Summary of Boundary Conditions Used To Calculate the Flow Profile and Limiting Currents in the MJE Simulation**

parabolic flow at inlet	$0 \leq r \leq r_T$	$z = H + 500$	$u_z = (2\hat{U}/r_T^2)r^2; u_r = 0$
plug flow at inlet	$0 \leq r \leq r_T$	$z = H$	$u_z = \hat{U}; u_r = 0$
constant $u_r$ at back wall of cell	$r_T \leq r \leq l$	$z = H$	$u_r = (V_0/2\pi r_T H)r^{-1}$
walls	$r = r_T$	$H \leq z \leq H + 500$	$u_z = 0; u_r = 0$
	$r_T \leq r \leq l$	$z = H$	
	$r_{elec} \leq r \leq l$	$z = 0$	
electrode	$0 \leq r \leq r_{elec}$	$z = 0$	$u_z = 0; u_r = 0$
centerline	$r = 0$	$0 \leq z \leq H + 500$	$u_r = 0$
bulk concentration at inlet	$0 \leq r \leq r_T$	$z = H + 500$	$a_{r,z} = a_0$
no concentration at electrode surface	$0 \leq r \leq r_{elec}$	$z = 0$	$a_{r,z} = 0$

element simulation to attain conditions close to either the idealized or more realistic conditions given in points i and ii above.

When parabolic flow at the nozzle exit was required, a parabolic value of  $u_z$  was applied at the start of the nozzle, as defined in Table 3. In the cases where it was desired to approximate plug flow, friction between the solution and the inlet walls tends to force the flow to develop a parabolic shape, so all of mesh face 1 (which represents the nozzle) was removed from the model and a constant value of  $u_z$  was applied across the inlet.

The boundary condition of constant  $u_r$  extending from the inlet wall down to the hydrodynamic layer cannot be imposed using FIDAP, which allows for boundary conditions to apply only on the external edges of the simulation. The closest condition that can be imposed is to impose a value of  $u_r$  at the wall at  $z = H$ , parallel to the one in which the electrode is embedded. This value falls in proportion with  $r^{-1}$ , while the conservation of flow is maintained. The initial value of this velocity was calculated as the mean flow in the  $r$ -direction, if the flow was assumed to maintain the jet shape it has in the nozzle over the full height of the cell.

The remaining two boundary conditions were consistent between the idealized and more realistic model. Both  $u_z$  and  $u_r$  were set to zero at boundaries specified as walls or as the electrode. At the centerline, the radial velocity must be zero. Apart from the above, it is unnecessary to specify any further boundary conditions at any other part of the cell (for example, no boundary condition for flow need be specified at the outlet). All of the above boundary conditions are summarized and expressed mathematically in Table 3.

**Flux Simulation.** As noted, in addition to solving the flow equations for a given geometry, FIDAP can then be used to solve the mass transport conditions operating at the MJE under limiting current conditions. The same mesh was used to calculate the flux to the electrode as was used to calculate the flow. To increase computational efficiency, the calculation of flux of species to the electrode was carried out using the fixed  $r$  and  $z$  fluid velocities taken from the flow solution. As concentrations involved were small, the flow pattern would not be altered by changes in the species concentration.

The flux calculations require two concentration-related boundary conditions to be imposed. Bulk concentration was imposed at the inlet and a boundary condition of zero concentration was imposed at the electrode surface to simulate limiting current conditions. These flux-related boundary conditions are also summarized in Table 3.

The introduction of electrochemistry in the simulation of the MJE leads to one other difference between the finite element solution and the analytical approach. The analytical approach of Albery and Bruckenstein neglects the effect of radial diffusion, as this is considered to be tiny compared to radial convection and diffusion normal to the electrode in the case of a WTE. However, diffusion edge effects cannot be ignored on the UME scale. FIDAP allows the calculation of diffusion with the radial contribution removed, so the contribution can be quantified.

The physical properties of the simulated solution were chosen to correspond with an aqueous solution<sup>13</sup> at 298 K, using a density of  $0.998 \text{ g cm}^{-3}$  and a dynamic viscosity of  $0.00888 \text{ cm}^2 \text{ s}^{-1}$ . When calculating the flux, a bulk concentration of  $2 \times 10^{-6} \text{ mol cm}^{-3}$  and diffusion coefficient of  $6.5 \times 10^{-6} \text{ cm}^2 \text{ s}^{-1}$  were used.

**TABLE 4: Cell Parameters and Node Information Used To Create the Meshes That Calculated the Limiting Currents in Figures 8–10<sup>a</sup>**

figure	$r_{\text{elec}}/\mu\text{m}$	$r_T/\mu\text{m}$	$H/\mu\text{m}$	$l/\mu\text{m}$	$V_f/\text{cm}^3 \text{ s}^{-1}$	no. of elements
8i, 9i	12.5	45	200	600	0.0045–0.019	8207
8ii, 9ii	12.5	58	300	600	0.016–0.043	8207
10	12.5	55	110–510	600	0.0338	8207–11805

<sup>a</sup> Definitions: radius of electrode,  $r_{\text{elec}}$ ; radius of inlet tube,  $r_T$ ; cell height,  $H$ ; centerline outlet distance,  $l$ ; volume flow rate,  $V_f$ .

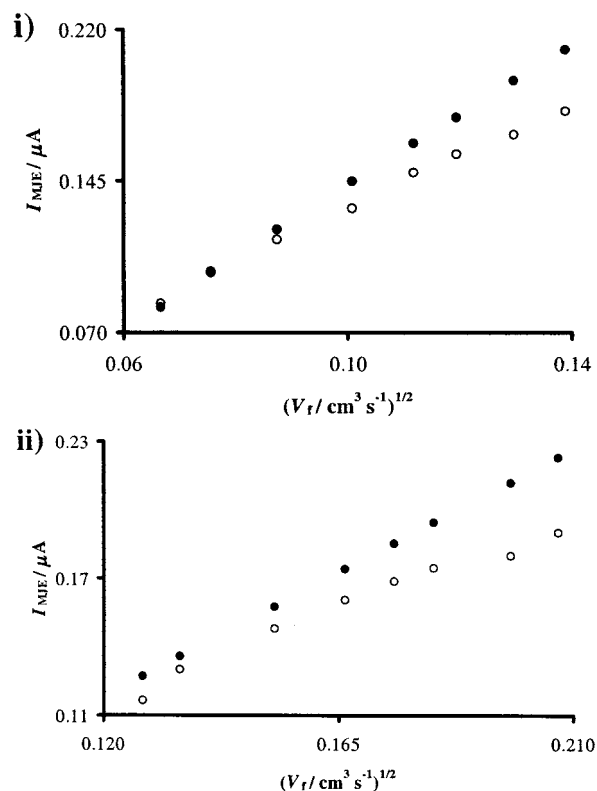
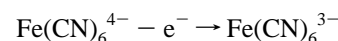


**Figure 8.** Comparison of experimental transport-limited current-flow rate data (open circles) with results obtained by finite element simulation (closed circles) at a  $12.5 \mu\text{m}$  radius UME. Data relates to (i)  $r_T = 45 \mu\text{m}$  and  $H = 200 \mu\text{m}$  and (ii)  $r_T = 58 \mu\text{m}$  and  $H = 300 \mu\text{m}$ .

## Results and Discussion

To establish the applicability of the FIDAP approach, a series of simulations were compared to previously published experimental work<sup>6</sup> involving a simple one-electron transfer process, the oxidation of hexacyanoferrate(II) ions in aqueous solution:



A series of simulations were run with varying volume flow rate for the first two cell geometries specified in Table 4. The results are shown in Figure 8. The moderate discrepancy between the published results and the FIDAP solution over the range of  $V_f$  for both geometries shows the general applicability of the finite difference approach to the microjet regime.

An advantage of using a finite element numerical solution is that each of the three “unrealistic” conditions employed when assuming Homann’s axisymmetric stagnation flow exists in the MJE (as specified in the Introduction) can be added to the standard model and their individual effect evaluated. The simulations were re-run three times using the geometries that produced Figure 8. With each run, one of the three simplifying assumptions that apply in the analytical approach—(i) plug flow

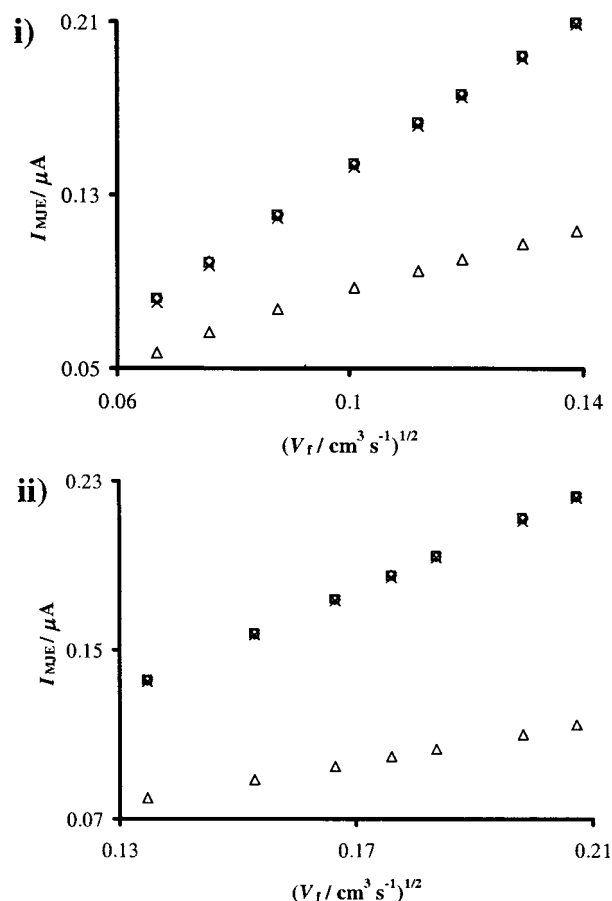


**Figure 9.** Comparison of the relative effects of each simplifying assumption when assuming axisymmetric flow with stagnation on the finite element transport-limited current-flow rate data from Figure 8. The diamonds show the full numerical solution, the squares the predicted response when radial diffusion is removed from the contribution to the flux to the electrode, the crosses the result of adding the constant  $u_r$  boundary to the back wall, and the triangles the effect of plug flow rather than parabolic flow. Data relates to (i)  $r_T = 45 \mu\text{m}$  and  $H = 200 \mu\text{m}$  and (ii)  $r_T = 58 \mu\text{m}$  and  $H = 300 \mu\text{m}$ . For both geometries,  $r_{\text{elec}} = 12.5 \mu\text{m}$ .

**TABLE 5: MJE Cell Parameters Used To Investigate Dependence of  $r$  and  $z$  on  $u_r$  and  $u_z$**

radius of electrode, $r_{\text{elec}}/\mu\text{m}$	radius of inlet tube, $r_T/\mu\text{m}$	cell height, $H/\mu\text{m}$	centerline outlet distance, $l/\mu\text{m}$
25	52	300	600

at the inlet, (ii) applying a constant value of  $u_r$  at  $(r_T, H)$ , or (iii) removal of the contribution of radial diffusion to the total flux to the electrode—was included with the other two replaced by the more “realistic” conditions specified in the previous section. The results are shown in Figure 9.

It can be seen from the graphs that there is negligible effect on the limiting current by removing the contribution from radial diffusion. Therefore, at these values of  $V_f$  and  $r_{\text{elec}}$  it is reasonable to neglect this contribution. However, at even lower values of  $r_{\text{elec}}$ , there may be a significant contribution from radial diffusion, and further work is planned to investigate this.

**TABLE 6: Distances for Which  $u_z \propto z^2$  and  $u_r \propto r$  at Different Values of  $V_f$**

$V_f/\text{cm}^3 \text{ s}^{-1}$	distance from electrode for which $u_z \propto z^2/\mu\text{m}$	distance from centerline for which $u_r \propto r/\mu\text{m}$	distance from electrode for which $u_r \propto z/\mu\text{m}$	range of $C/10^4 \text{ cm}^{-1} \text{ s}^{-1}$
0.000825	100	75	21	2.0–9.0
0.003	25	40	5	140–300
0.0165	5	35	1	1900–20000
0.03	4	35	1	3800–57000
0.3	1	20	0	400–18000

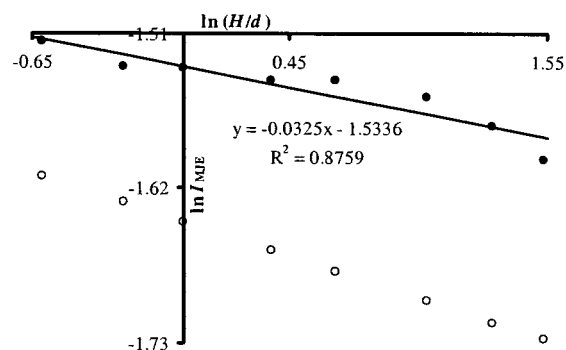


**Figure 10.** The effect of the nozzle-electrode distance,  $H$ , on the transport-limited current, shown as a log plot. The data were generated using a nozzle radius of  $55 \mu\text{m}$ , a  $12.5 \mu\text{m}$  radius UME, and a volume flow rate of  $0.0338 \text{ cm}^3 \text{ s}^{-1}$ . The closed circles show the currents generated by the finite element numerical solution and the open circles the currents predicted for a conventional-sized WTE.

The addition of the constant  $u_r$  boundary condition at the back wall does affect the flow profile in that region. The effect is most pronounced at low flow rates. However, close to the electrode surface (within  $20 \mu\text{m}$ ), the difference in both radial and axial velocities was always less than 2%, and this caused a maximum 1.8% difference to the limiting current when compared to simulations run without this boundary condition. For most flow rates (when  $V_f \geq 10^{-2} \text{ cm}^3 \text{ s}^{-1}$  at both geometries studied), this difference was less than 1%.

However, replacing the parabolic flow profile with plug flow resulted in a marked reduction in the limiting current. This comes about due to there being proportionally more volume at the sides of the plug flow compared to a parabolic distribution. This results in there being less volume impinging on the electrode at any time, due to the width of the flow being much wider than the electrode diameter. This flow will also be at a smaller velocity, and these two effects result in a lower flux to the electrode in a given time, and hence, the current is reduced. This result suggests that the assumption of uniform accessibility due to  $u_z$  being independent of  $r$  is the biggest cause of discrepancy between WTE theory and the results obtained by finite element numerical solution.

A series of simulations were next run to obtain limiting currents for direct comparison with the observations of Chin and Tsang, who found an empirical dependence of the normalized electrode-nozzle length of  $(H/d)^{-0.054}$  on the transport-limited current in the region  $0.2 < (H/d) < 6.0$  in the case of a conventionally sized wall tube electrode. A series of numerical simulations were run in the  $(H/d)$  region with a nozzle radius,  $r_T = 55 \mu\text{m}$ ,  $r_{\text{elec}} = 12.5 \mu\text{m}$ , and a  $V_f$  of  $0.0338 \text{ cm}^3 \text{ s}^{-1}$ . The viscosity, density, and diffusion coefficient associated with the fluid were the same as specified in the previous section. The nozzle to electrode distance was set at 60, 85, 110, 160, 210, 310, 410, and  $510 \mu\text{m}$  and the flux obtained at each height converted to a limiting current. The results are displayed as the log plot in Figure 10.

The open circles represent the response predicted by Chin and Tsang's empirical observations and the closed circles the

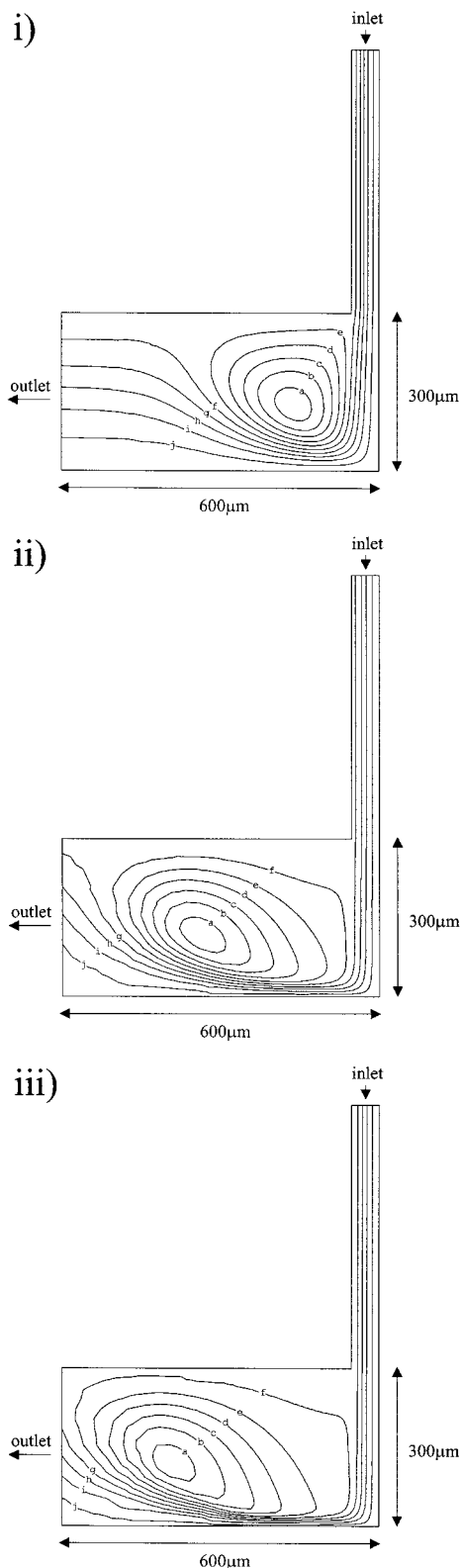


**Figure 11.** A plot of the streamlines in the MJE, illustrating the presence of a vortex, for three volume flow rates: (i)  $0.003 \text{ cm}^3 \text{ s}^{-1}$  (figure legend/ $\text{cm s}^{-1}$ : a,  $-0.5787 \times 10^{-2}$ ; b,  $-0.5177 \times 10^{-2}$ ; c,  $-0.4568 \times 10^{-2}$ ; d,  $-0.3959 \times 10^{-2}$ ; e,  $-0.3350 \times 10^{-2}$ ; f,  $-0.2741 \times 10^{-2}$ ; g,  $-0.2132 \times 10^{-2}$ ; h,  $-0.1523 \times 10^{-2}$ ; i,  $-0.9137 \times 10^{-2}$ ; j,  $-0.3046 \times 10^{-3}$ ); (ii)  $0.03 \text{ cm}^3 \text{ s}^{-1}$  (figure legend/ $\text{cm s}^{-1}$ : a,  $-0.7555 \times 10^{-1}$ ; b,  $-0.6759 \times 10^{-1}$ ; c,  $-0.5964 \times 10^{-1}$ ; d,  $-0.5169 \times 10^{-1}$ ; e,  $-0.4374 \times 10^{-1}$ ; f,  $-0.3578 \times 10^{-1}$ ; g,  $-0.2783 \times 10^{-1}$ ; h,  $-0.1988 \times 10^{-1}$ ; i,  $-0.1193 \times 10^{-1}$ ; j,  $-0.3976 \times 10^{-2}$ ); (iii)  $0.3 \text{ cm}^3 \text{ s}^{-1}$  (figure legend/ $\text{cm s}^{-1}$ : a,  $-0.6785$ ; b,  $-0.6071$ ; c,  $-0.5357$ ; d,  $-0.4642$ ; e,  $-0.3928$ ; f,  $-0.3214$ ; g,  $-0.2500$ ; h,  $-0.1786$ ; i,  $-0.1071$ ; j,  $-0.3571 \times 10^{-1}$ ).

results obtained from FIDAP. The FIDAP results clearly do not follow a  $(H/d)^{-0.054}$  relation. The best fit line suggests a relation of  $(H/d)^{-0.033}$ , but the  $R^2$  value clearly indicates that there is no true linear relation between  $\ln(H/d)$  and  $\ln i_{\text{MJE}}$ , as predicted by Chin and Tsang. Experimental results<sup>6</sup> show a similar curvature to that of the FIDAP log plot, rather than a straight line. This suggests that this particular empirical observation of Chin and Tsang at conventional-sized WTEs is inappropriate at the MJE scale.

Having established the applicability of the finite element approach to predict limiting currents for a typical MJE geometry and flow regime, it was next used to verify or otherwise eqs 6 and 7 when applied to MJE. Simulations were run at a series of volume flow rates between  $8.25 \times 10^{-3}$  and  $3.00 \times 10^{-1} \text{ cm}^3 \text{ s}^{-1}$  using the cell geometry parameters specified in Table 5 and the physical quantities stated in the previous section. These runs were carried out without attempting to apply either of the idealizations assumed to apply in stagnation flow, i.e., the simulation was run using a parabolic flow profile at the nozzle exit, and there was no attempt to apply a constant value of  $u_r$  on the flow as it leaves the nozzle.

Once the simulation has run, velocities at each node can be obtained. log plots of velocity against distance were then plotted using these data. There were three sets of plots taken:

- (i)  $\ln |u_z|$  against  $\ln z$  at fixed  $r$  between  $r = 0$  and  $50 \mu\text{m}$ ;
- (ii)  $\ln |u_r|$  against  $\ln r$  at fixed  $z$  between  $z = 1$  and  $20 \mu\text{m}$ ;
- (iii)  $\ln |u_r|$  against  $\ln z$  at fixed  $r$  between  $r = 0$  and  $50 \mu\text{m}$ .

To ascertain how far in the radial and axial directions the velocity–distance proportionalities described in eqs 6 and 7 pertain, several different log plots of each type were obtained by varying the value that  $r$  (in the case of plot types i and iii) or  $z$  (for plots of type ii) was fixed at. Plots of  $\log |u_z|$  and  $\log |u_r|$  against  $\log z$  were obtained at  $r = 0, 1, 10, 20, 30, 40$ , and  $50 \mu\text{m}$ , corresponding to two radii away from the electrode center in the axial direction. Plots of  $\log |u_r|$  against  $\log r$  were obtained at  $z = 1, 2, 4, 6, 8$ , and  $10 \mu\text{m}$  above the electrode surface.

For plots of  $\log |u_z|$  against  $r$ , a straight line with a gradient of 2 near the origin would be confirmation of the order of proportionality given in eq 6. For verification of the order of proportionality in eq 7, both plots of  $\log |u_r|$  against  $\log r$  and  $\log z$  should produce straight lines of gradient 1 near the origin. It was considered that the relationship  $u_z \propto z^2$  applied over the distance from the electrode when the gradient of the plot of  $\log |u_z|$  against  $z$  was between 2 and 1.9. In the case of  $u_r \propto r$  and  $u_z \propto r$ , the proportionality was considered to no longer apply when the gradient became less than 0.95.

Table 6 summarizes the extent of agreement of  $u_z = Cz^2$  and  $u_r = Crz$  where  $C$  is the constant of proportionality, identified as  $1.31\alpha^{3/2}\nu^{-1/2}$  by Froessling.  $C$  was calculated from the finite element simulation as the exponential of the intercept of the straight line part of the log plots, allowing a separate calculation of  $C$  for each plot.

It can be seen from Table 6 that the simulation provides no evidence of a constant value of  $C$  in the hydrodynamic boundary layer, as predicted by Froessling and used by Albery and Bruckenstein to derive eq 14.  $C$  instead depends on the value of  $r$  and  $z$  at which the log plots are obtained.  $C$  also differs depending on the volume flow rate, but this can be attributed to the effect of  $\alpha$ , the hydrodynamic constant, which varies with  $V_f$ .

Another major difference between the flow pattern predicted by the theory of Froessling and results obtained by finite element simulation is the existence of a vortex in the MJE. This is



illustrated by a series of streamline plots at three different flow rates (0.003, 0.03, and  $0.3 \text{ cm}^3 \text{ s}^{-1}$ ), presented in panels i–iii of Figure 11, respectively. It can be seen that the center of the vortex begins to move toward the outlet at high flow rate, but at low values of  $V_f$ , there is a possibility that the position of the vortex could result in an enhanced flow to the electrode, above that predicted by the work of Froessling.

## Conclusions

The finite element approach to the solution of the flow in and flux to the MJE has been shown to produce trends comparable to experimental results with satisfactory agreement. Analysis of the velocity profile near the electrode surface has shown significant deviations from the analytical solution that applies to the WTE derived by Alberty and Bruckenstein, and comparison of how limiting current changes with nozzle-electrode distance has shown deviation from the empirical observations of Chin and Tsang. The assumption of plug flow, necessary to apply the conditions of Homann's axisymmetrical stagnation flow in the analytical solution, has been shown to have a very large effect on the predicted limiting current when compared to a more realistic parabolic flow. Future work,

including investigating the effect of ignoring radial diffusion when using smaller electrodes, the effect of nozzle wall thickness, and offsetting the electrode from the center of the cell, is envisaged.

## References and Notes

- (1) Tani, I.; Komatsu, Y. *Proceedings of the 11th International Congress of Applied Mechanics*; Gortler, H., Ed.; Springer-Verlag, 1966.
- (2) Strand, T. AIAA Paper No. 64-424.
- (3) Glauert, M. B. *J. Fluid. Mech.* **1956**, *1*, 625.
- (4) Chin, D.-T.; Tsang, C.-H. *J. Electrochem. Soc.* **1978**, *125*, 1463.
- (5) Yamada, J.; Matsuda, H. *J. Electroanal. Chem.* **1973**, *44*, 189.
- (6) Macpherson, J. V.; Marcar, S.; Unwin, P. R. *Anal. Chem.* **1994**, *66*, 2175.
- (7) Martin, R. D.; Unwin, P. R. *J. Electroanal. Chem.* **1995**, *397*, 325.
- (8) Macpherson, J. V.; Beeston, M. A.; Unwin, P. R. *J. Chem. Soc., Faraday Trans.* **1995**, *91*, 899.
- (9) cited in Schlichting, H. *Boundary Layer Theory*; McGraw-Hill: New York, 1960; pp 81–83.
- (10) Alberty, J. W.; Bruckenstein, S. *J. Electroanal. Chem.* **1983**, *144*, 105.
- (11) Marken, F.; Tsai Y. C.; Coles B. A.; Matthews S. L.; Compton, R. G. *New J. Chem.* **2000**, *24*, 653.
- (12) Fulian, Q.; Coles, B. A.; Marken, F.; Compton, R. G. *J. Electroanal. Chem.* **2000**, *492*, 150.
- (13) *CRC Handbook of Chemistry and Physics*, 55<sup>th</sup> ed.; Weast, R. C., Ed.; CRC Press: Cleveland, OH, 1974.